Highly ordered Pd/CeOx inverse opals for alkaline hydrogen oxidation

Downloaded from: https://research.chalmers.se, 2026-10-12 15:15 UTC

Citation for the original published paper (version of record):
Wilms, M., Ya'u Musa, A., Raju, R. et al (2026). Highly ordered Pd/CeOx inverse opals for alkaline hydrogen oxidation. Nanoscale, 18(21): 11347-11357. http://dx.doi.org/10.1039/d6nr00422a

N.B. When citing this work, cite the original published paper.

research.chalmers.se offers the possibility of retrieving research publications produced at Chalmers University of Technology. It covers all kind of research output: articles, dissertations, conference papers, reports etc. since 2004. research.chalmers.se is administrated and maintained by Chalmers Library

(article starts on next page)

Nanoscale

PAPER

Published on 06 May 2026
Licensed under CC-BY 4.0

Check for updates

Cite this: *Nanoscale*, 2026, **18**, 11347

Highly ordered Pd/CeO_x inverse opals for alkaline hydrogen oxidation

Michael Wilms, [a,b] Arma Musa Yau,[a,b] Ruby Susan Raju,[a] Deya Sallaberry[a] and Mathilde Luneau *[a,b]

Palladium supported on ceria (Pd/CeO_x) has recently emerged as a promising electrocatalyst for the alkaline hydrogen oxidation reaction (HOR) in anion exchange membrane fuel cells. It has been proposed that CeO_x provides OH spillover and modulates Pd–H binding, enhancing the reaction kinetics at the key Pd–Ce interface. Herein, we report a method to maximise the Pd–Ce interfacial area by synthesising highly ordered Pd/CeO_x inverse opals (IOs) with tunable pore sizes (20–250 nm) directly on glassy carbon electrodes. The resulting IOs exhibit highly ordered pore networks which could be scaled down to the mesoporous regime (<50 nm), and dispersed palladium species, including Pd–O–Ce interfacial sites. Electrochemical measurements reveal a pore size dependence of HOR activity, with IOs fabricated from 104 nm microspheres templates delivering the highest specific activity and strongest enhancement relative to non-templated Pd/CeO_x controls. Electrochemically active surface area (ECSA) estimations reveal that larger-pore IOs suffer reduced ECSA likely due to diminished support conductivity associated with thinner ceria interconnections. Increasing the Ce^{3+} concentration, in an effort to improve conductivity, and increasing relative Pd–O–Ce content do not improve HOR activity, highlighting the need to balance conductivity, Pd and Ce speciation and pore size. The Pd/CeO_x IOs remain structurally stable after testing and interestingly, even exhibit improved kinetics after 1000 cycles. This study demonstrates that while the inverse opal architecture is a powerful route to engineer Pd–Ce interfaces, these interfaces are not the only predictor of enhanced HOR. Instead, the inverse opal pore size and interconnect thickness appear to ultimately govern the enhanced HOR kinetics and mass transport. We envision that this fabrication method for inverse opals on complex carbon substrates will allow the design of mesoporous bifunctional catalysts for gas-diffusion electrodes for applications in fuel cells and electrolyzers.

Received 30th January 2026,
Accepted 17th April 2026

DOI: 10.1039/d6nr00422a

rsc.li/nanoscale

Introduction

Hydrogen fuel cells have seen major advancements over the past few decades and show strong potential to replace internal combustion engines in heavy-duty vehicles.[1] Proton exchange membrane fuel cells (PEMFCs) are the most advanced low temperature fuel cell technology but have seen limited commercial uptake. The main drawbacks preventing their widespread adoption are acidic environment induced instability of electrodes and sluggish kinetics of the oxygen reduction reaction (ORR) at the cathode.[2] This limits the catalyst choice to platinum which constitutes roughly 40% of the total cell cost.[3]

Anion exchange membrane fuel cells (AEMFCs) have emerged as a promising alternative with a less corrosive cell environment allowing a wider choice of catalysts such as nickel, palladium and other non-platinum group metals (PGMs).[4–6] The ORR also becomes significantly enhanced in alkaline conditions, eliminating the key bottleneck in operating efficiency in PEMFCs.[7] However, the switch to alkaline conditions in turn leads to sluggish kinetics in the hydrogen oxidation reaction (HOR) at the anode which is *ca.* 100 times slower than in acidic media due to the reaction now requiring adsorption of both hydrogen and hydroxyl anions.[8,9] Now it has been suggested that in an ideal alkaline HOR catalyst, the hydroxide binding energy (OHBE) must be modulated as well as the hydrogen binding energy (HBE).[10] In this regard palladium supported on ceria (CeO_x) has emerged as a promising catalyst as CeO_x could act as an oxyphilic OH^- donor and the metal–support interactions can modulate the hydrogen binding energy of palladium.[10–12] It has been proposed that the spillover effect of OH intermediates on oxyphillic CeO_x to supported palladium and the weakened Pd–H bond is the key mechanism in Pd/CeO_x leading to superior HOR performance in alkaline.[13] This has led to the development of state-of-the-art Pd–C/CeO_2 catalyst achieving power densities of 1.4 W

[a]*Department of Chemistry and Chemical Engineering, Chalmers University of Technology, Gothenburg 412 96, Sweden. E-mail: mathilde.luneau@chalmers.se*
[b]*Competence Centre for Catalysis (KCK), Chalmers University of Technology, Gothenburg 412 96, Sweden*

cm^{-2}.[14] More recent structure–activity studies have found that maximizing the interface area between Pd and CeO_x is key in encouraging the spillover effect of OH intermediates thereby increasing HOR performance.[15] However to date, studies focusing on maximizing the Pd–Ce interface have only focused on unstructured CeO_x. This study aims to explore structured Pd/CeO_x with increased surface area and porosity of the CeO_x support, giving potential to maximize the total desired Pd–Ce interface.

Inverse opals offer a promising strategy for designing highly porous and ordered metal–oxide supports such as CeO_2 and related materials.[16,17] These honeycomb-like structures feature well defined pore networks formed by the self-assembly of colloidal spheres into an FCC lattice, followed by infiltration with a precursor solution and subsequent removal of the template to yield the final 'inverse opal' architecture.[18] To date, most research on inverse opals has focused on their structural color as photonic crystals for optical applications or use in photocatalysis and thermocatalysis.[19–23] Their application in electrocatalysis has only recently gained attention, yet current studies remain limited to bulk monometallic or bimetallic systems such as Cu,[24] Ni,[25] Ag,[26] CuAg[27] and NiFe.[28] While these systems have shown enhanced electrocatalytic performances, using bulk metals limits their atom efficiency in contrast with the low loading supported-metal bifunctional materials like Pd/CeO_x proposed in this study. Moreover, it is difficult to reliably scale the pore size of inverse opals down to the mesoporous (2–50 nm) regime that is characteristic of high-surface-area carbons used in real-world electrochemical technologies such as fuel cells and batteries.[29,30] CeO_x specifically lacks reliable synthesis routes for generating mesoporous materials like those for SiO_2. Furthermore, to our knowledge there is no example of mixed material inverse opal such as a classical support–metal catalyst system for electrocatalytic applications.

Mathilde Luneau

Dr Mathilde Luneau is an Assistant Professor at the Department of Chemistry and Chemical Engineering at Chalmers University of Technology in Gothenburg, Sweden. Before joining Chalmers University of Technology, she was a postdoctoral fellow at Harvard University, USA in the group of Prof. Cynthia Friend. Mathilde obtained her PhD from the University of Lyon 1, France in 2016 where she worked at the Institute of Research on Catalysis and Environment (IRCELyon). Her current research focuses on the design of novel catalytic materials and novel reactors for applications in electrocatalytic and thermocatalytic reactions.

In this work, we synthesized novel highly ordered Pd/CeO_x inverse opals (IOs) with tunable pore sizes directly onto glassy carbon disks for the first time, with the aim of maximizing the Pd–Ce interfacial area and enhancing mass transport through the porous network. Using a modified vertical assembly approach, we produced IOs with pore sizes determined by the diameter of the colloidal spheres (510 nm, 380 nm, and 104 nm) achieving pore sizes of 250 nm down into the mesoporous regime (20–50 nm) while maintaining consistent palladium loading and Pd–Ce interfacial area throughout the porous support architecture. We found the Pd/CeO_x IOs with mesopores (104 nm spheres) yielded the best hydrogen oxidation performance with exchange current densities of 0.067 mA cm^{-2} compared to 0.061 mA cm^{-2} and 0.027 mA cm^{-2} for unstructured Pd/CeO_x and macroporous 380 nm IO respectively. Pd–Ce interfacial area was further improved by template removal *via* argon annealing instead of calcination in air, which produced mixed performance improvements across the different IO morphologies, indicating pore size is a better predictor of HOR activity than Pd speciation. Long-term potential cycling revealed that the hydrogen oxidation kinetics of Pd/CeO_x improved over time with X-ray photoelectron spectroscopy showing a near equal re-balancing of Pd species (Pd (0), PdO and Pd–O–Ce) which could explain the improved kinetics.

Experimental

General

All solvents and reagents were supplied from commercially available sources and used without purification. Polystyrene microspheres (carboxyl terminated) of sizes 104 nm, 380 nm and 510 nm were acquired from Polysciences. Glassy carbon electrodes with a 5 mm diameter (Sigradur®) disks were purchased from HTW GmbH.

Fabrication of palladium on ceria inverse opals

Pd/CeO_x inverse opals were fabricated using a modified vertical deposition method (VPD, Scheme 1). Glassy carbon electrodes (GCE) were first cleaned by submerging in base piranha (3 : 1 $NH_3OH : H_2O_2$) at 60 °C for 20 minutes. To improve the hydrophilicity, GCEs were kept submerged in 1.5 M HCl and used no earlier than 24 hours after treatment time. For glassy carbon disks where 104 nm microspheres were self-assembled, an additional treatment of polyamine hydrochloride was performed to prevent peeling of the template from the GCE surface. The polystyrene microspheres of various sizes (185 μL, 2.7% solids) were diluted to 5 mL in a 20 mL glass sample vial to make a 0.1% solids dispersion. The freshly cleaned GCE was then mounted on a glass slide using carbon tape and submerged in the vial containing the PS dispersion such that the GCE surface was perpendicular to the middle of the solution meniscus. The vial was then placed in a convection oven at 60 °C for 24 hours to allow the evaporation of water and self-assembly of polystyrene microspheres. A 15 wt% Pd precursor

This journal is © The Royal Society of Chemistry 2026

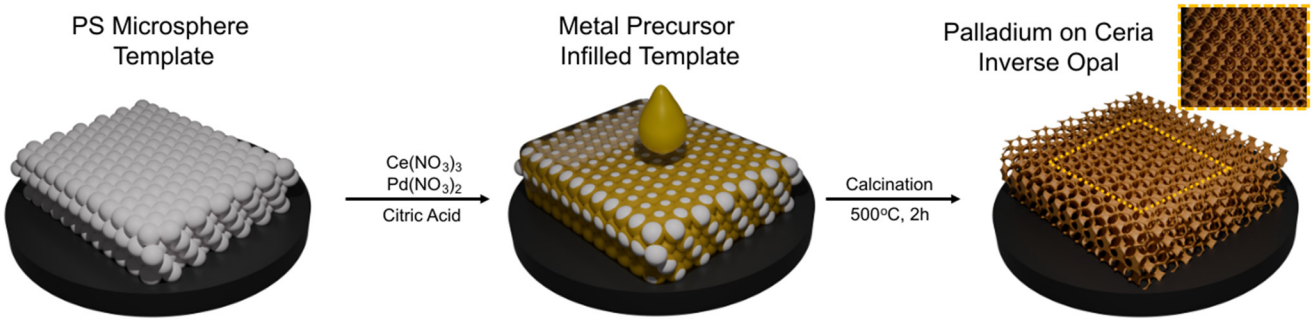

Scheme 1 Fabrication scheme of Pd/CeO_x inverse opals. Polystyrene microspheres were first self-assembled onto a glassy carbon electrode followed by infiltration with $Ce(NO_3)_3$ and $Pd(NO_3)_2$ precursor solution and subsequent calcination yielding metal–support bifunctional inverse opals.

solution was prepared by dissolving $Ce(NO_3)_3{\cdot}6H_2O$ (172.1 mg, 0.40 mmol), $Pd(NO_3)_2{\cdot}xH_2O$ (26.3 mg, 0.11 mmol) and citric acid (83.2 mg, 0.43 mmol) in ethanol (2.42 mL). HCl (100 μL, 12.07 M) was subsequently added to homogenise the solution. The 15 wt% Pd precusor was then used for the infiltration step unless otherwise stated. The inverse opal templates were then infiltrated with 2.5 μL of this precursor solution and aged for 24 hours. The infilled templates were then heated to 150 °C at a ramp rate of 1 °C min^{-1} then immediately calcined at a ramp rate of 5 °C min^{-1} to the target temperature and held for 2 hours yielding Pd/CeO_x inverse opals. The no opal samples were synthesized using the same method but without self-assembly of the polystyrene microsphere template.

Preparation of Pd thin films

Thin films were fabricated using electron-beam physical vapor deposition (AVAC HVC600) on GCEs. Prior to deposition, the electrodes were cleaned by sonication in acetone, isopropanol and Milli-Q water (18.2 MU cm) for 10 minutes each and dried with N_2 followed by plasma cleaning in O_2 atmosphere at 100 W for 1 minute. After cleaning, a 20 nm Ti underlayer was deposited to improve adhesion of the Pd. The pure Pd sample was prepared by evaporating a 40 nm Pd thin film on the Ti adhesion layer. The electrodes had a geometrical surface area of 0.196 cm^2 as with the IO samples.

Instruments

Transmission electron microscopy (TEM) samples were prepared by placing a GCE supported IO face down in a vial with minimum ethanol to coat the base off the vial. The vial was then sonicated to remove the top layer of material from the GCE surface. The IO ethanol solution was then dropcasted onto a 300-mesh carbon-coated copper grids (Ted Pella) and left until the solvent evaporated. TEM images were acquired on a FEI T20 Tecnai microscope operating at 100 kV. X-ray photoelectron spectroscopy (XPS) was performed using a HI5000 Versa Probe III XPS equipped with a monochromatic AlKα source and dual charge compensation was used during acquisition. XPS spectra were calibrated with respect adventitious carbon C1s peak (284.5 eV). For scanning electron microscopy (SEM) imaging, the samples fabricated on GCE electrodes were imaged directly using a Zeiss Ultra 55 FEG SEM operating at 3 kV in order to reduce charging. Energy dispersive spectroscopy (EDX) measurements were carried out using a JEOL 7800F Prime operating at 15 kV.

Electrochemical measurements

The Pd/CeO_x IO electrodes were electrochemically tested using a three-electrode setup in a single polytetrafluoroethylene (PTFE) cell. A rotating disk electrode with a geometric area of 0.196 cm^2 was used as the working electrode, a graphitic carbon rod served as the counter electrode, and Hg/HgO was used as the reference electrode. Cyclic voltammetry (CV) and hydrogen oxidation reaction were performed in 0.1 M KOH electrolyte at room temperature. All potentials are reported against RHE which was determined to be −0.869 V *vs.* Hg/HgO by using a Pt counter electrode and a Pt working electrode while flowing H_2 gas.

To estimate the electrochemically active surface area (ECSA), CO stripping was not used as it has been shown in previous work that Pd adatoms on ceria (Pd–O–Ce) cannot adsorb CO onto its surface.[12] Another common method, integration of the PdO reduction charge, was not used as the peak in the cyclic voltammogram is difficult to observe in electrodes with high CeO_x loading due to extreme capacitive behaviour of CeO_2.[31] Instead, copper underpotential deposition (UPD) was used which has been used previously to approximate the ECSA of PtPd alloys.[32] The ECSA measurements were carried out in 0.25 M H_2SO_4. The samples were first conditioned by potential cycling 20 times between −0.2 V and 0.7 V (*vs.* Ag/AgCl) at a scan rate of 50 mV s^{-1}. The sample background was then measured between 0.05 and 0.66 V followed by the addition of solid $CuSO_4$ (to make up a 160 mM solution) before scanning cathodically from 0.66 to 0.05 V to form the Cu monolayer, while the reverse scan corresponded to the Cu monolayer stripping current. The Cu stripping current is integrated to yield total stripping charge which is proportional to the electrochemically active surface area by:

$$\mathrm{ECSA}\,(\mathrm{cm}^2) = \frac{Q_{\mathrm{Cu}}}{424\,\mu\mathrm{C\,cm}^{-2}}$$

where 424 μC cm^{-2} corresponds to the anodic stripping charge

of a fully-packed copper monolayer from the surface of palladium.[32]

Results and discussion

Material characterizations

The modified vertical deposition method (VPD) developed here yielded highly ordered inverse opal templates for all microsphere sizes yielding an FCC packing arrangement with visual opalescence occurring in the 380 nm and 510 nm microsphere templates. This showcases the robustness of the method in fabricating inverse opals on rough surfaces like graphitic carbon which is relevant for fuel cell applications. Next the opal polymer template was infilled with a metal precursor solution. This process yielded Pd/CeO_x inverse opals with tuneable pore sizes by varying polymer microspheres sizes between 510 nm, 330 nm and 104 nm (Fig. 1a–c). The inverse opals form as "islands" throughout the GCE film rather than a continuous film, which is expected when using a non-colloidal VPD strategy (Fig. S1).

A pre-baking step of 150 °C was employed to induce thermal shrinkage of the PS template by exceeding the glass-transition temperature of the PS microsphere. The deliberate softening allows for the reduction of pore size below the microsphere diameter while concomitantly increasing interconnect width, which we suspect governs the bulk conductivity of the electrode. While this process slightly reduces long range order over the area of the electrode, the 510 nm and 330 nm microspheres still yielded highly ordered macroporous inverse opals of 225 ± 26 nm and 147 ± 32 nm diameter with interconnect widths 28 ± 6 nm and 76 ± 16 nm respectively (Fig. S2). For the 104 nm microspheres, the pore sizes were too small to measure a size distribution with SEM, however, they estimated to fall within the 20–50 nm range. This confirms that this method can be used to produce IOs in the mesoporous regime for the first time. This is especially important considering it is difficult to synthesize polymer microspheres below 100 nm with a low enough polydispersity index to form colloidal crystal templates.

SEM/EDX measurements revealed that the palladium was well incorporated throughout the ceria inverse opal matrix (Fig. 1d–g and Fig. S3). The Pd/Ce ratios given by EDX for samples in Fig. 1 were in decent agreement with nominal weight percentages used in the precursor solutions and importantly, was consistent across all morphologies (Fig. S3 and Table S1). EDX over different sample regions showed only a few occurrences of larger Pd particles over the IO support. Instead, most Pd that occurs in maps was homogeneously contained within the IO framework, suggesting they could be present as few or single atom sites. Pd/CeO_x samples calcined at the lower temperatures of 300 °C and 400 °C showed the formation of Pd and PdO nanoparticles, indicating that a calcination temperature of 500 °C is necessary to achieve high Pd dispersion (additional discussion can be found in the SI, Fig. S5). Transmission electron microscopy analysis supports this conclusion, showing no evidence of larger Pd nanoparticle formation on the IO framework (Fig. 2a–c). High resolution TEM

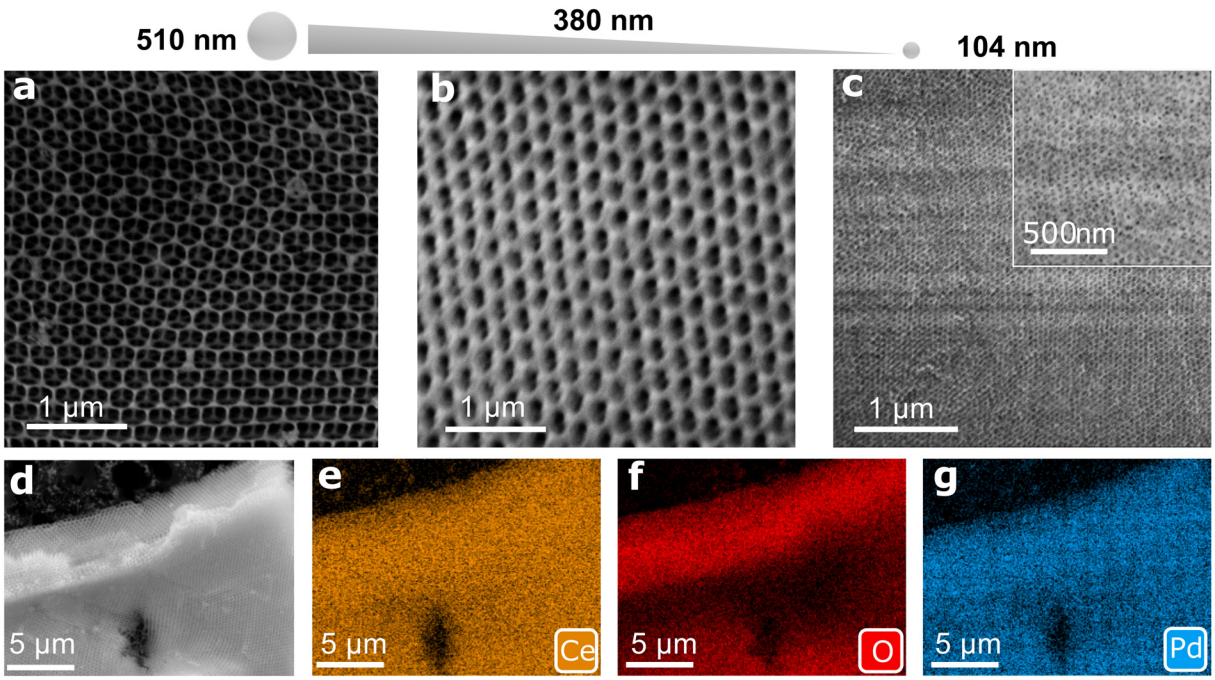

Fig. 1 Highly ordered Pd/CeO_x inverse opals were synthesized as shown by SEM micrographs using polymer microsphere sizes of (a) 510 nm, (b) 380 nm and (c) 104 nm. Low magnification SEM image of 380 nm Pd/CeO_x IO and corresponding energy dispersive spectroscopy elemental maps (d–g) showing uniform distribution of Pd throughout the porous CeO_x framework.

This journal is © The Royal Society of Chemistry 2026

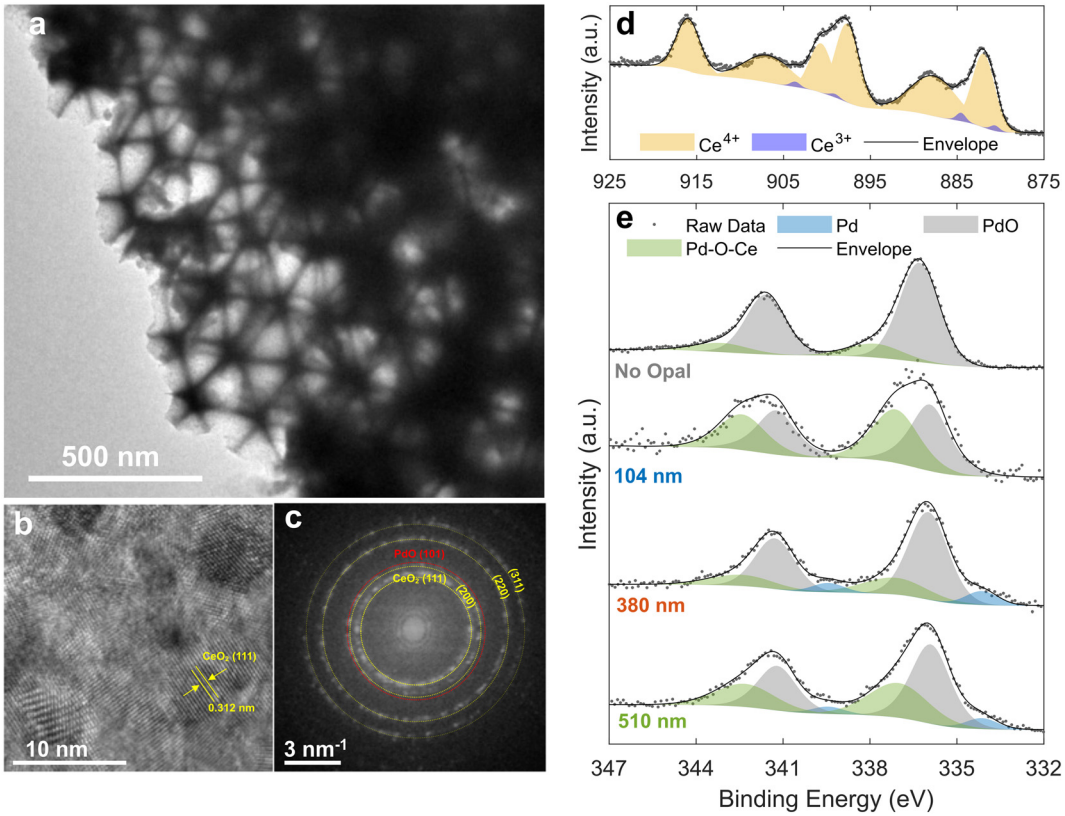

Fig. 2 (a) TEM image of the 510 nm Pd/CeO_x IO collected in bright field mode. (b) HR-TEM of Pd/CeO_x 510 nm IO showing main lattice fringe of CeO_x (111). (c) FFT analysis of HR-TEM showing diffraction rings of CeO_2 and faint PdO (101) fringe. X-ray photoelectron spectroscopy of the (d) Ce3d region (104 nm IO) and (e) Pd3d region of Pd/CeO_x inverse opals.

(HR-TEM) imaging showed no presence of large Pd or PdO crystallites. Only the main lattice fringe of CeO_2 was observed (111). FFT analysis of the HR-TEM images revealed a very faint ring corresponding to PdO (101), while no rings corresponding to Pd (111) were detected. It was not possible to resolve the other bright PdO lattice fringe (112), as it strongly overlaps with the CeO_2 (311) plane. To investigate the origin of the PdO (101) ring in the absence of large observable PdO crystallites, we conducted line-profile analysis of the CeO_2 crystallites. This analysis revealed possible Pd substitutions within the lattice, evidenced by a reduction in the (111) lattice parameter from 0.31 nm down to 0.26 nm, which matches the spacing of PdO (101) (Fig. S4). This suggests that some PdO could be incorporated as single atoms or clusters within the CeO_x matrix instead of spatially co-located.

X-ray photoelectron spectroscopy was performed to determine the speciation of Pd in the IOs and the stoichiometry of the ceria support. The XPS Pd3d spectrum 5/2 spin orbit peak shows two components situated at 336.1 ± 0.3 eV and 337.4 ± 0.3 eV corresponding to Pd–O and Pd–O–Ce respectively.[33,34] Some samples required a minor metallic Pd component at 334.5 ± 0.3 eV to obtain the best fit (Fig. 2d, e and Table S2). The presence of the Pd–O–Ce peak was consistent with Pd atoms being covalently bonded to CeO_x. In our previous work, density functional theory calculations revealed this covalent Pd–O–Ce species is "embedded" into the CeO_x lattice.[12] This same species constitutes the proposed Pd–Ce interface that has been widely cited as a key physical descriptor underpinning the strong HOR performance of Pd/CeO_x.[31] The Ce3d region exhibited peaks mainly corresponding to Ce^{4+}. The best Ce3d fit was obtained when a minimal Ce^{3+} component was introduced, indicating the ceria framework is slightly non-stoichiometric, which has been shown to increase conductivity through defects within the CeO_x lattice (Fig. 2d).[35]

Electrochemical measurements of calcined Pd/CeO_x inverse opals

The redox behaviour of palladium in argon atmosphere is heavily influenced by the underlying CeO_x support. Cyclic voltammograms of an unsupported palladium thin film show PdO_x reduction at *ca.* 0.7 V *vs.* RHE (Fig. 3a). Hydrogen adsorption/absorption occurs between 0.2–0.0 V *vs.* RHE (cathodic) with oxidation/desorption then occurring in the same region in the anodic scan. The CV of Pd/CeO_x IOs shows a more pronounced Pd oxidation peak although the reduction peak is almost totally obscured by the background of the ceria support which has been observed for Pd/CeO_x with high ceria content.[31]

The HOR activity of the Pd/CeO_x IO was significantly higher than that of the unsupported Pd film. The latter reached a

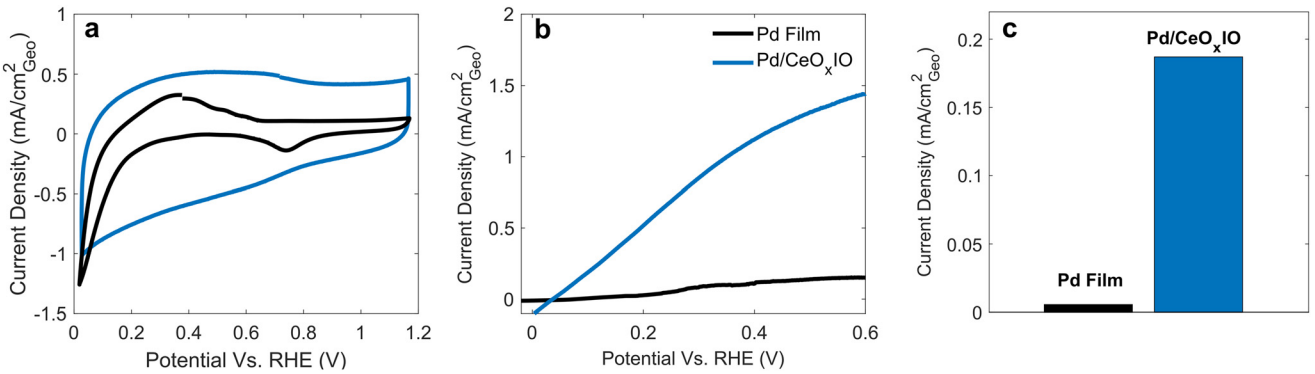

Fig. 3 (a) Cyclic voltammetry of evaporated Pd film (black) and 104 nm Pd/CeO_x inverse opal (blue) at a scan rate of 100 mV s^{-1} and in argon atmosphere in 0.1 M KOH electrolyte. (b) Anodic HOR sweeps at a scan rate of 5 mV s^{-1} at a rotation speed of 1600 RPM in saturated H_2 atmosphere in 0.1 M KOH electrolyte. (c) Current density at an overpotential of 0.1 V *vs.* RHE.

diffusion-limited plateau at approximately 0.6 V *vs.* RHE, whereas the IOs achieved a plateau at a lower potential of approximately 0.45 V *vs.* RHE (Fig. 3b). Although we note that the limiting current plateau is not sharply defined, this deviation from Levich behaviour is likely caused by the thickness and porosity of the IO framework, influencing mass transport resistance.[36] At an overpotential of 0.1 V *vs.* RHE, little current is observed for the Pd film, while the Pd/CeO_x inverse opals demonstrated improved current density by a factor of 10, (Fig. 3c) highlighting the strong positive effect of the ceria support on Pd HOR activity, as observed in other works.[12] For a pristine CeO_x IO with no Pd, almost no current was observed in HOR, further demonstrating the positive metal–support interaction between Pd and CeO_x (Fig. S6).

The HOR performance of Pd/CeO_x was heavily influenced by morphology which was examined using 15 wt% of palladium with ceria by nominal loading in precursor solutions. Cyclic voltammograms of the different IOs in argon atmosphere showed similar redox behaviour as palladium supported on ceria (Fig. 4a). However the inverse opal samples displayed a strong dependence on pore size: mesoporous IOs prepared using 104 nm microspheres delivered the highest HOR activity across the full potential range, followed by the 380 nm and 510 nm macroporous structures (Fig. 4b and c). In contrast, Pd/CeO_x without an inverse opal architecture showed reduced current at both low overpotentials and in the diffusion-controlled region, indicating that both kinetics and mass transport were significantly improved in the mesoporous IO (104 nm, Fig. 4b) compared to the unstructured electrocatalyst. It was observed that the current density decreased with increasing pore size, which could be due to the thinner ceria backbone in larger pore IOs, leading to reduced overall conductivity of the support. Therefore, when working with intrinsically low conductivity supports such as CeO_x, a balance must be struck between pore size and electronic conductivity to achieve optimal HOR performance.

To explore this further, the electrochemically active surface area (ECSA) was measured for all electrode morphologies. Initially double layer capacitance from cyclic voltammetry was explored, however the non-faradaic double layer region is difficult to resolve in CeO_x supported Pd due to the highly capacitive nature of CeO_x, making it not feasible to accurately estimate ECSA. CO stripping voltammetry was also evaluated for ECSA determination, however a DFT study in our previous work shows "embedded" palladium (Pd–O–Ce) cannot adsorb CO, making it potentially invisible in this technique.[12] Therefore, we turned to copper under-potential deposition (CuUPD) which has been widely used as a highly accurate method of measuring ECSA, particularly for catalysts dispersed on high surface area supports.[32,37] CuUPD measurements revealed surprisingly Pd/CeO_x with no opal morphology hosted the highest ECSA followed by 104 nm sample with ECSA substantially decreasing as pore size increased (Fig. 4d and Fig. S7). While it may seem surprising that the more porous samples exhibit lower electrochemically active surface area, this is likely due to reduced conductivity in the thicker, more hollow support frameworks. In thicker structures, the upper layers of the inverse opal likely have a low contribution to overall charge transport in the electrode, and the overall contact area between the framework and the glassy carbon electrode is reduced. As discussed earlier, larger pore sizes correspond to thinner interconnect structures, which aligns with the observed trend in decreasing ECSA. However, when normalizing the HOR current to the ECSA derived from CuUPD, the specific activity at 0.1 V *vs.* RHE was highest for the 380 nm inverse opal, followed by the 104 nm and no opal anode (Fig. S8a). This suggests that the electrochemically active sites may be intrinsically more efficient for hydrogen oxidation in the intermediate pore-size regime. In the mass-transport regime, the 104 nm IO and 380 nm IO achieve >5 mA $cm^{-2}{}_{Pd}$ and >10 mA $cm^{-2}{}_{Pd}$. These values represent a 5- and 10-fold increase over the no opal sample, suggesting that the IO architecture could be a viable Pd/CeO_x morphology for AEMFCs if the total ECSA can be increased. Relative surface area measurements derived from the capacitance in cyclic voltammetry also showed the same morphological trend as in CuUPD (Table S3). However, when normalizing for the capacitance derived ECSA, it is observed that 104 nm IO is the most

 This journal is © The Royal Society of Chemistry 2026

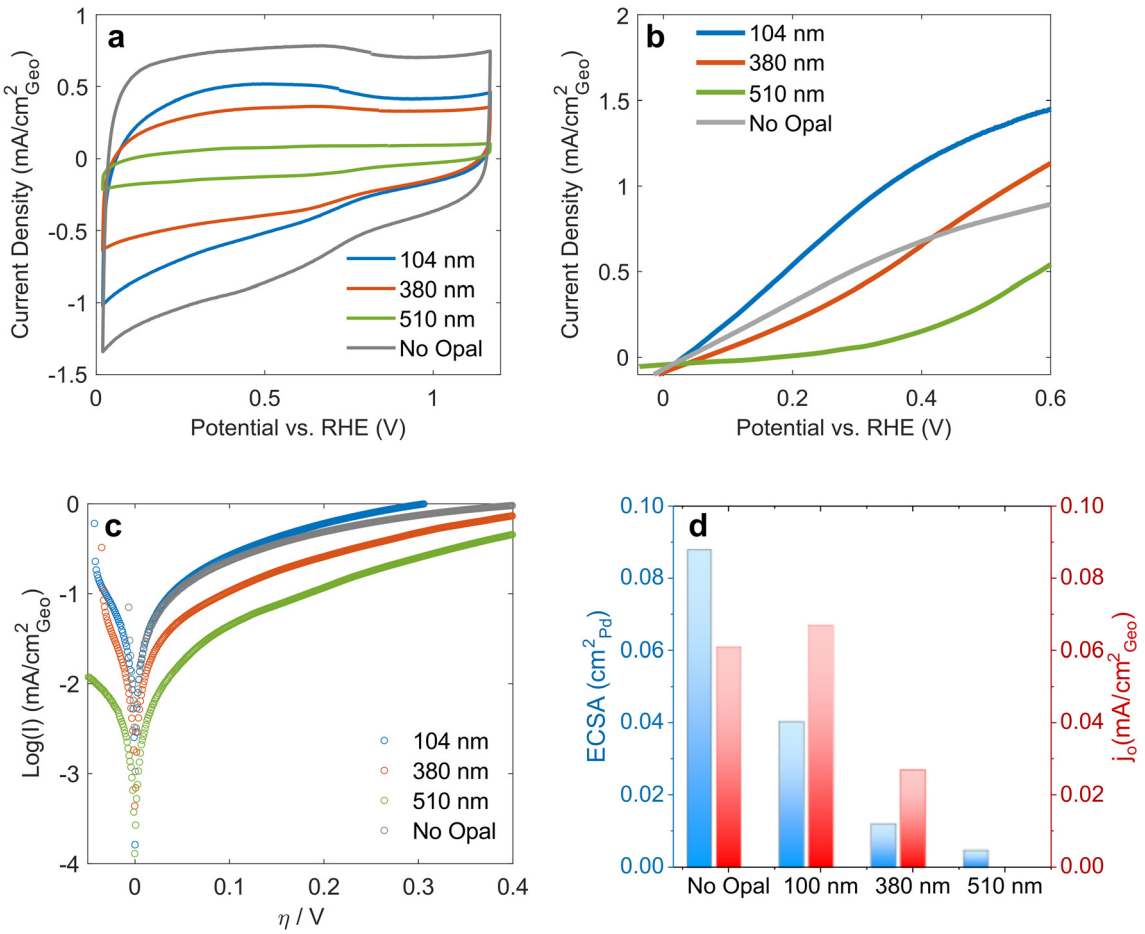

Fig. 4 (a) Cyclic voltammetry of Pd/CeO_x inverse opals fabricated using different template sizes, along with a non-templated control, recorded using a scan rate of 100 mV s^{-1} under argon atmosphere in 0.1 M KOH electrolyte. (b) Anodic HOR sweeps recorded using a scan rate of 5 mV s^{-1} at a rotation speed of 1600 RPM under saturated H_2 atmosphere in 0.1 M KOH electrolyte. (c) Tafel plots of anodic HOR sweeps recorded at 5 mV s^{-1} and 1600 RPM under saturated H_2 atmosphere in 0.1 M KOH electrolyte. (d) Electrochemically active surface area (cm^2_{Pd}) and exchange current density (mA cm^{-2}) of Pd/CeO_x IOs.

electrochemically active for HOR (Fig. S8b). The half-wave potentials were also observed to be approximately the same across these three morphologies (0.16–0.2 V *vs.* RHE) while the 510 nm opal exceeds 0.6 V *vs.* RHE, exceeding that of pristine Pd (Fig. 4b).

The exchange currents densities of the Pd/CeO_x IOs were found to have a similar morphological trend as the ECSA with the exception of the 104 nm IO, which exhibited the highest exchange current density (Fig. 4d). Exchange currents were estimated by approximating the Butler–Volmer equation to a linear equation $i_k = i_0 \frac{F\eta}{RT}$ in the micropolarization region where i_k is the kinetic current, i_0 is the exchange current, F is Faraday's constant (96 485 C mol^{-1}), R is the gas constant (8.413 J mol^{-1} K^{-1}) and T is temperature (K).[38] HOR curves within the micropolarization region clearly indicate the 104 nm IO architecture exhibits superior charge-transfer kinetics compared to both the non-templated (No opal) and the 380 nm IO samples (Fig. S9). This was further supported by the exchange current densities (j_0), which revealed the 104 nm IO achieves the highest j_0 among the investigated morphologies (0.067 mA cm^{-2}) (Fig. 4d).

To improve conductivity and increase Pd–Ce interfacial area, thereby enhancing HOR performance, different annealing and template-removal conditions were explored. First, oxygen vacancies were introduced into the ceria framework by annealing in an inert argon atmosphere. The inverse opal structure was preserved after template removal in argon, except for the 380 nm sample, which was found to have a highly disordered pore morphology (Fig. S10). XPS analysis revealed an observable increase in the Ce^{3+}/Ce^{4+} ratio as anticipated (Fig. S11) suggesting the successful introduction of oxygen vacancies into near-surface and bulk. We note that oxygen vacancies only persist in near surface and bulk regions, as oxygen vacancies present at the surface are rapidly healed under ambient conditions. Therefore, this experiment was intended solely to enhance the conductivity of the bulk ceria framework rather than to modify surface reactivity, which is

not achievable under ambient conditions, as previously highlighted by Idriss.[39]

The XPS Pd3d spectrum shows a significant increase of the Pd–O–Ce content for all morphologies with only minor PdO (<10%) and remainder corresponding to Pd(0) (Fig. S12 and S13). Interestingly the Pd–O–Ce content increases with pore size, with the 104 nm and no opal sample having the lowest percentage (19.5% and 49.5%) and 380 nm and 510 nm the highest (50.9% and 79.62%). This trend correlates with SEM observations, which revealed Pd nanoparticles in the 104 nm and 380 nm IOs, but not in the 510 nm IO. This consistent decrease in Pd(0) suggests that pore size influences Pd nanoparticle morphology during argon annealing. Furthermore, these results indicate that the inverse opal architecture may enhance the Pd–Ce interface area when appropriate template removal conditions are employed in combination optimal pore size (Tables S4 and S5). The HOR performance of argon annealed inverse opals was found to increase in both the kinetic control and mass transport region for the 380 nm and no opal samples (Fig. S14). Curiously, despite having a greater proportion of Pd–O–Ce/Pd(0) ratio to the air calcined counterparts, both the 104 nm and 510 nm IOs saw performance decreases, suggesting the Pd–O–Ce/Pd(0) ratio is not the sole indicator of performance. We note that other works have had Pd/CeO_x supported on carbon forming a triple interface between C/Pd/Ce, adding more complexity to the system which could explain these discrepancies. Overall, these results suggest that the role of the triple interface warrants closer attention, rather than focusing exclusively on the Pd–Ce interface.

Long term stability of calcined Pd/CeO_x IO

The long-term stability of the Pd/CeO_x inverse opals was assessed by testing HOR performance before and after potential cycling. Remarkably, it was found that HOR performance increased after 1000 potential cycles between 0 V to 1.2 V *vs.* RHE (Fig. 5a and b). In all samples the specific activity at 0.1 V *vs.* RHE increased by >5% with half wave potentials also decreasing (Fig. S15) The 104 nm IO saw almost a 50% improvement in exchange current density from 0.067 mA cm^{-2} to 0.096 mA cm^{-2} (Fig. S16). While the kinetics clearly improved, there was a current loss observed in the mass trans-

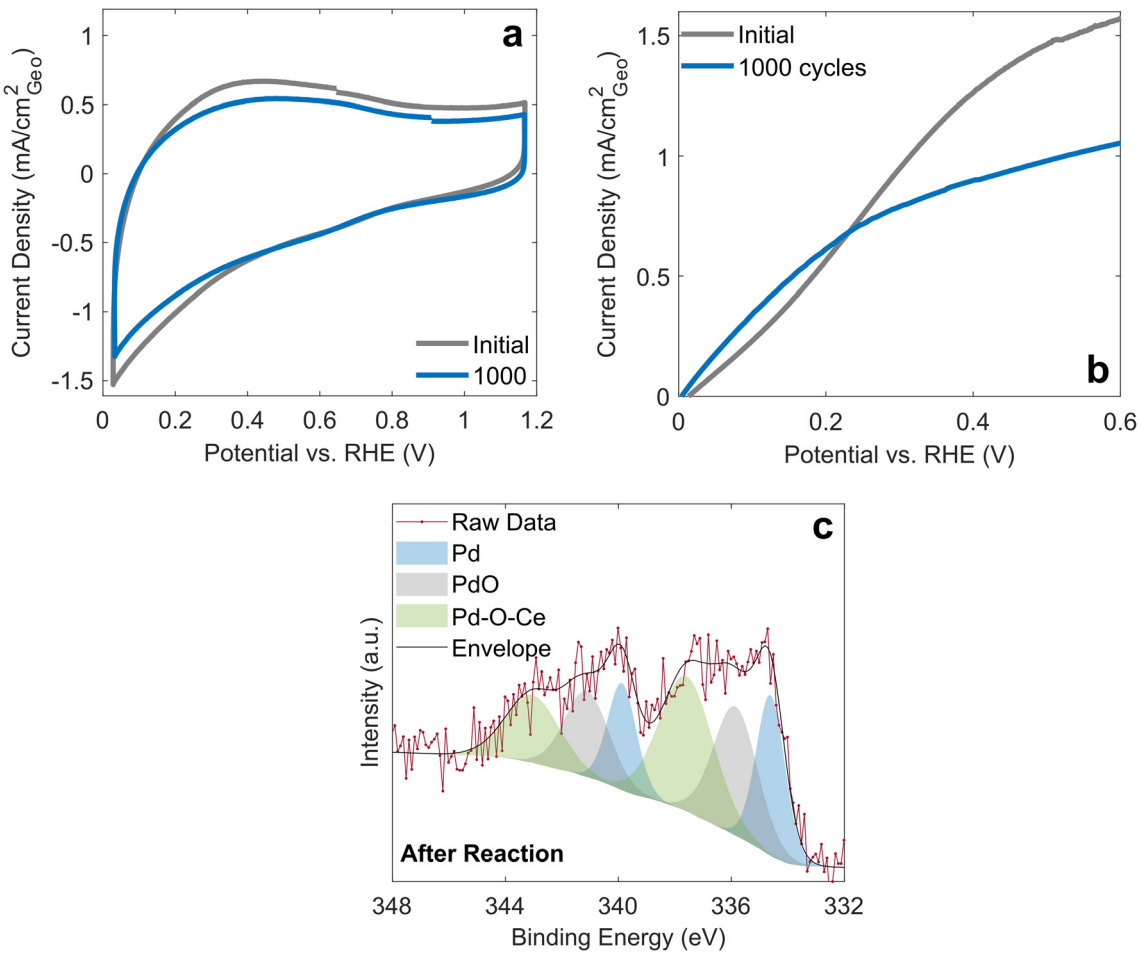

Fig. 5 (a) Cyclic voltammogram (initial and 1000th cycle) of Pd/CeO_x inverse opal fabricated using 104 nm PS microspheres at a scan rate of 100 mV s^{-1} under argon atmosphere in 0.1 M KOH electrolyte. (b) Anodic HOR sweeps before potential cycling (initial) and after 1000th potential cycle in 0.1 M KOH electrolyte. XPS Pd3d region of 104 nm IO (c) after 1000th potential cycle.

This journal is © The Royal Society of Chemistry 2026

port-controlled region suggesting some ECSA loss after potential cycling. Although another hypothesis was that Pd imbedded in the ceria framework reorganises/rearranges to the ceria inverse opal surface increasing surface-active Pd. This concomitantly decreased the overall conductivity of the support which leads to the loss of current in the mass transport region but improved kinetics in the activation region. We performed SEM to verify if this was simply due to a change in morphology and found that the IO pores were retained after cycling (Fig. S17).

XPS analysis revealed that the surface speciation of Pd/CeO_x changes considerably after potential cycling (Fig. 5c). After cycling, metallic Pd(0) was observed, along with PdO and Pd–O–Ce in similar percentages (27.3%, 33.8% and 38.9% respectively) which has also been observed for planar Pd/CeO_x films after potential cycling.[12] These results suggest that the presence of all three Pd species may influence HOR performance. Notably, the total percentage of the Pd–O–Ce speciation decreased after cycling (from 48.2% to 38.9%) despite HOR kinetics improving. This dynamic restructuring after cycling clearly shows that it is difficult to ascribe HOR performance to a particular Pd speciation. As discussed previously, the Ar annealed IOs which exhibited enhanced Pd–O–Ce content to their air calcined counterparts saw either a reduction in HOR kinetics or a marginal increase which might further decouple Pd–O–Ce content as a sole predictor for HOR activity. Furthermore, the surface composition of Pd/CeO_x is likely very dynamic under potential cycling and under constant current output conditions during AEMFC operation. Therefore, future work must utilize operando XPS to definitively identify the optimal surface composition under varying potentials to better understand the dynamic nature of the Pd/CeO_x surface during reaction.

Conclusion

The growth of mesoporous Pd/CeO_x inverse opals directly onto glassy carbon electrodes was successfully demonstrated for the first time using a modified vertical self-assembly approach. By changing the sizes of the polymer microspheres, the pore sizes were tuned from 250 nm down to the mesoporous regime (<50 nm). EDX and XPS analysis revealed that palladium appeared to be homogenously dispersed throughout the architecture and was predominantly present as Pd–O and Pd–O–Ce species (~10–40%). HOR performance was found to be strongly governed by morphology where IOs made using 104 nm microspheres yielded the best performance compared to the larger pore inverse opals and notably against the unstructured no opal Pd/CeO_x electrodes. Electrochemically active surface area (ECSA) measurements performed with Cu UPD show a loss of ECSA with increasing pore size and the highest with no opal electrode suggesting the differences in HOR performance arises from a loss of conductivity in the larger pore inverse opals which concomitantly feature smaller backbone widths. Argon annealing was found to significantly improve the percentage of Pd–O–Ce and Ce^{3+} suggesting defect-induced conductivity improves in CeO_x and Pd–Ce interfacial area. However, this did not lead to improvements in HOR performance and was in fact detrimental to the performance of the better performing samples (104 nm and no opal). Finally, long-term potential cycling revealed that IOs maintain their structural features and even exhibit improved activation-controlled kinetics, suggesting dynamic restructuring of Pd within the CeO_x framework under potential cycling. This work establishes inverse-opal structuring as a versatile approach for engineering Pd–Ce interfaces, while allowing fine control of pore size and morphology leading to improved HOR performance in both the kinetic and mass transport regime. We envision this strategy could also be useful for engineering Pd–Ce interfaces combined with macro/meso-porous materials particularly for other fields such as thermocatalysis where framework conductance is not a limiting factor.

Author contributions

ML guided the research. MW wrote the paper. MW conducted the synthesis and collected the TEM and SEM images. MW performed the XPS analysis and electrochemical tests. AYM fabricated planar Pd films. AYM, DS and RSR helped with collecting preliminary results.

Conflicts of interest

There are no conflicting interests to declare.

Data availability

The authors confirm that the data supporting the results of this work are available within the article and the provided supplementary information (SI). Supplementary information is available. See DOI: https://doi.org/10.1039/d6nr00422a.

Raw data are available upon request.

Acknowledgements

We would like to acknowledge Professor Elisabet Ahlgren for assistance with capacitance measurements and her fruitful discussions and Dr Christine Geers for assistance with Argon annealing of electrodes. We acknowledge the Area of Advance Energy, Chalmers University of Technology for financial support. The Competence Centre for Catalysis is hosted by Chalmers University of Technology and financially supported by the Swedish Energy Agency (Project No. 52689-1) and the member companies Johnson Matthey, Perstorp, Powercell, Preem, Scania CV, Umicore, and Volvo Group. We acknowledge the staff of Myfab Chalmers and the Chalmers Materials Analysis Laboratory (CMAL) where physical characterizations were carried out.

References

1 D. A. Cullen, K. C. Neyerlin, R. K. Ahluwalia, R. Mukundan, K. L. More, R. L. Borup, *et al.*, New roads and challenges for fuel cells in heavy-duty transportation, *Nat. Energy*, 2021, **6**(5), 462–474.

2 H. Cruz-Martínez, H. Rojas-Chávez, P. T. Matadamas-Ortiz, J. C. Ortiz-Herrera, E. López-Chávez, O. Solorza-Feria, *et al.*, Current progress of Pt-based ORR electrocatalysts for PEMFCs: An integrated view combining theory and experiment, *Mater. Today Phys.*, 2021, **19**, 100406.

3 W. Gibbons, G. Kleen and J. Fornaciari, DOE Hydrogen and Fuel Cells Program Record, Heavy-Duty Fuel Cell System Cost, 2023.

4 P. Eskandari, S. Zhou, J. Yuwono, D. Gunawan, R. F. Webster, Z. Ma, *et al.*, Enhanced Hydrogen Evolution Reaction in Alkaline Media via Ruthenium–Chromium Atomic Pairs Modified Ruthenium Nanoparticles, *Adv. Mater.*, 2025, **37**(34), 2419360.

5 W. Ni, T. Wang, F. Héroguel, A. Krammer, S. Lee, L. Yao, *et al.*, An efficient nickel hydrogen oxidation catalyst for hydroxide exchange membrane fuel cells, *Nat. Mater.*, 2022, **21**(7), 804–810.

6 H. Liu, Z. Zhang, M. Li, Y. Li, Y. Kuang and X. Sun, Ru-doped WO3 enabling efficient hydrogen oxidation reaction in alkaline media, *Nanoscale*, 2023, **15**(28), 12064–12070.

7 Y. Sun, S. Polani, F. Luo, S. Ott, P. Strasser and F. Dionigi, Advancements in cathode catalyst and cathode layer design for proton exchange membrane fuel cells, *Nat. Commun.*, 2021, **12**(1), 5984.

8 J. Durst, A. Siebel, C. Simon, F. Hasché, J. Herranz and H. A. Gasteiger, New insights into the electrochemical hydrogen oxidation and evolution reaction mechanism, *Energy Environ. Sci.*, 2014, **7**(7), 2255–2260.

9 W. Sheng, H. A. Gasteiger and Y. Shao-Horn, Hydrogen Oxidation and Evolution Reaction Kinetics on Platinum: Acid vs Alkaline Electrolytes, *J. Electrochem. Soc.*, 2010, **157**(11), B1529.

10 D. Strmcnik, M. Uchimura, C. Wang, R. Subbaraman, N. Danilovic, D. van der Vliet, *et al.*, Improving the hydrogen oxidation reaction rate by promotion of hydroxyl adsorption, *Nat. Chem.*, 2013, **5**(4), 300–306.

11 N. Ralbag, E. S. Davydova, M. Mann-Lahav, P. Cong, J. He, A. M. Beale, *et al.*, Ceria Entrapped Palladium Novel Composites for Hydrogen Oxidation Reaction in Alkaline Medium, *J. Electrochem. Soc.*, 2020, **167**(5), 054514.

12 M. Luneau, L. Strandberg, G. Montserrat-Sisó, V. Shokhen, R. Mohan, H. Grönbeck, *et al.*, Fundamental insight into enhanced activity of Pd/CeO_2 thin films in hydrogen oxidation reaction in alkaline media, *J. Mater. Chem. A*, 2023, **11**(30), 16370–16382.

13 H. A. Miller, A. Lavacchi, F. Vizza, M. Marelli, F. Di Benedetto, F. D'Acapito, *et al.*, A Pd/C-CeO_2 Anode Catalyst for High-Performance Platinum-Free Anion Exchange Membrane Fuel Cells, *Angew. Chem., Int. Ed.*, 2016, **55**(20), 6004–6007.

14 M. Bellini, M. V. Pagliaro, A. Lenarda, P. Fornasiero, M. Marelli, C. Evangelisti, *et al.*, Palladium–Ceria Catalysts with Enhanced Alkaline Hydrogen Oxidation Activity for Anion Exchange Membrane Fuel Cells, *ACS Appl. Energy Mater.*, 2019, **2**(7), 4999–5008.

15 R. K. Singh, E. S. Davydova, J. Douglin, A. O. Godoy, H. Tan, M. Bellini, *et al.*, Synthesis of CeOx-Decorated Pd/C Catalysts by Controlled Surface Reactions for Hydrogen Oxidation in Anion Exchange Membrane Fuel Cells, *Adv. Funct. Mater.*, 2020, **30**(38), 2002087.

16 G. I. N. Waterhouse, J. B. Metson, H. Idriss and D. Sun-Waterhouse, Physical and Optical Properties of Inverse Opal CeO_2 Photonic Crystals, *Chem. Mater.*, 2008, **20**(3), 1183–1190.

17 X. Zhang, C. Weinberger, S. Amrehn, X. Wu, M. Tiemann and T. Wagner, Synthesis of Metal Oxide Inverse Opals from Metal Nitrates by PMMA Colloidal Crystal Templating, *Eur. J. Inorg. Chem.*, 2020, **2020**(35), 3402–3407.

18 Y. S. Zhang, C. Zhu and Y. Xia, Inverse Opal Scaffolds and Their Biomedical Applications, *Adv. Mater.*, 2017, **29**(33), 1701115.

19 R. C. Schroden, M. Al-Daous, C. F. Blanford and A. Stein, Optical Properties of Inverse Opal Photonic Crystals, *Chem. Mater.*, 2002, **14**(8), 3305–3315.

20 M. Curti, J. Schneider, D. W. Bahnemann and C. B. Mendive, Inverse Opal Photonic Crystals as a Strategy to Improve Photocatalysis: Underexplored Questions, *J. Phys. Chem. Lett.*, 2015, **6**(19), 3903–3910.

21 M. Luneau, T. Shirman, A. C. Foucher, K. Duanmu, D. M. A. Verbart, P. Sautet, *et al.*, Achieving High Selectivity for Alkyne Hydrogenation at High Conversions with Compositionally Optimized PdAu Nanoparticle Catalysts in Raspberry Colloid-Templated SiO_2, *ACS Catal.*, 2020, **10**(1), 441–450.

22 M. Luneau, T. Shirman, A. Filie, J. Timoshenko, W. Chen, A. Trimpalis, *et al.*, Dilute Pd/Au Alloy Nanoparticles Embedded in Colloid-Templated Porous SiO_2: Stable Au-Based Oxidation Catalysts, *Chem. Mater.*, 2019, **31**(15), 5759–5768.

23 K. R. G. Lim, M. Aizenberg and J. Aizenberg, Raspberry-Colloid-Templated Catalysts as a Versatile and Stable Thermocatalytic Platform, *Acc. Chem. Res.*, 2025, **58**(21), 3259–3272.

24 X. Zheng, J. Han, Y. Fu, Y. Deng, Y. Liu, Y. Yang, *et al.*, Highly efficient CO2 reduction on ordered porous Cu electrode derived from Cu2O inverse opals, *Nano Energy*, 2018, **48**, 93–100.

25 Q. Zhou, J. Pu, X. Sun, C. Zhu, J. Li, J. Wang, *et al.*, In situ surface engineering of nickel inverse opal for enhanced overall electrocatalytic water splitting, *J. Mater. Chem. A*, 2017, **5**(28), 14873–14880.

26 V.-V. Ittersum, *Mater. Adv.*, 2025, **6**, 2588–2599.

27 M. E. T. Vink-van Ittersum, M. L. J. Peerlings, N. M. T. van de Ven, T. J. E. Heijnen, P. Ngene and P. E. de Jongh, Positioning Cu in Templated Porous Ag for Active and

 This journal is © The Royal Society of Chemistry 2026

Selective Electroreduction to C2+ Products, *ChemElectroChem*, 2025, **12**(23), e202500170.

28 T. D. Nguyen, L. Nguyen, K. Dinh, D. Van Zeil, J. J. Jasieniak, J. F. Varga, *et al.*, Design of the Low-Loading NiFe Hydroxide Alkaline Oxygen Evolution Catalyst Layers Based on Inverse Opal Supports, *ACS Appl. Mater. Interfaces*, 2025, **17**(45), 62064–62075.

29 J. W. Lee, J. Lee, C. Kim, C.-Y. Cho and J. H. Moon, Facile fabrication of sub-100 nm mesoscale inverse opal films and their application in dye-sensitized solar cell electrodes, *Sci. Rep.*, 2014, **4**(1), 6804.

30 S. R. Kousik, D. Sipp, K. Abitaev, Y. Li, T. Sottmann, K. Koynov, *et al.*, From Macro to Mesoporous ZnO Inverse Opals: Synthesis, Characterization and Tracer Diffusion Properties, *Nanomaterials*, 2021, **11**(1), 196.

31 H. Yu, E. S. Davydova, U. Ash, H. A. Miller, L. Bonville, D. R. Dekel, *et al.*, Palladium-ceria nanocatalyst for hydrogen oxidation in alkaline media: Optimization of the Pd–CeO_2 interface, *Nano Energy*, 2019, **57**, 820–826.

32 F. Fiçicioğlu and F. Kadirgan, Characterization of a Pt + Pd alloy electrode by underpotential deposition of copper, *J. Electroanal. Chem.*, 1993, **346**(1), 187–196.

33 V. Muravev, G. Spezzati, Y.-Q. Su, A. Parastaev, F.-K. Chiang, A. Longo, *et al.*, Interface dynamics of Pd–CeO_2 single-atom catalysts during CO oxidation, *Nat. Catal.*, 2021, **4**(6), 469–478.

34 K. R. Priolkar, P. Bera, P. R. Sarode, M. S. Hegde, S. Emura, R. Kumashiro, *et al.*, Formation of Ce1-xPdxO2-δ Solid Solution in Combustion-Synthesized Pd/CeO_2 Catalyst: XRD, XPS, and EXAFS Investigation, *Chem. Mater.*, 2002, **14**(5), 2120–2128.

35 T. Suzuki, I. Kosacki, H. U. Anderson and P. Colomban, Electrical Conductivity and Lattice Defects in Nanocrystalline Cerium Oxide Thin Films, *J. Am. Ceram. Soc.*, 2001, **84**(9), 2007–2014.

36 R. T. Bonnecaze, N. Mano, B. Nam and A. Heller, On the Behavior of the Porous Rotating Disk Electrode, *J. Electrochem. Soc.*, 2007, **154**(2), F44.

37 C. L. Green and A. Kucernak, Determination of the Platinum and Ruthenium Surface Areas in Platinum–Ruthenium Alloy Electrocatalysts by Underpotential Deposition of Copper. I. Unsupported Catalysts, *J. Phys. Chem. B*, 2002, **106**(5), 1036–1047.

38 P. J. Rheinländer, J. Herranz, J. Durst and H. A. Gasteiger, Kinetics of the Hydrogen Oxidation/Evolution Reaction on Polycrystalline Platinum in Alkaline Electrolyte Reaction Order with Respect to Hydrogen Pressure, *J. Electrochem. Soc.*, 2014, **161**(14), F1448.

39 H. Idriss, On the wrong assignment of the XPS O1s signal at 531–532 eV attributed to oxygen vacancies in photo- and electro-catalysts for water splitting and other materials applications, *Surf. Sci.*, 2021, **712**, 121894.

This journal is © The Royal Society of Chemistry 2026